

3D Raman image of a pharmaceutical ointment.

# 3D Raman Imaging

Turn ideas into **discoveries**

Let your discoveries lead the scientific future. Like no other system, WITec's confocal 3D Raman microscopes allow for cutting-edge chemical imaging and correlative microscopy with AFM, SNOM, SEM or Profilometry. Discuss your ideas with us at [info@witec.de](mailto:info@witec.de).





Raman · AFM · SNOM · RISE

[www.witec.de](http://www.witec.de)

## RESEARCH ARTICLE

# Theoretical methods for calculations of optical phonons in BiOBr: Analysis and correction of propagated errors

Mateus M. Ferrer<sup>1</sup>  | João Elias F.S. Rodrigues<sup>2</sup>  | Marcio A.P. Almeida<sup>3</sup> |  
Francisco Moura<sup>4</sup> | Elson Longo<sup>5</sup> | Paulo S. Pizani<sup>2</sup> | Julio R. Sambrano<sup>1</sup>

<sup>1</sup>Modeling and Molecular Simulations Group, São Paulo State University, UNESP, Bauru, SP 17033-360, Brazil

<sup>2</sup>Optical Spectroscopy and Raman Scattering Group, Federal University of São Carlos, São Carlos, SP 13565-905, Brazil

<sup>3</sup>Coordenação de Ciência de Tecnologia, Federal University of Maranhão, Bacanga, São Luís, MA 65085-580, Brazil

<sup>4</sup>Laboratório Interdisciplinar de Materiais Avançados, Federal University of Itajubá, UNIFEI, Itabira, MG 35903-087, Brazil

<sup>5</sup>CDMF-UNESP, São Paulo State University, UNESP, Araraquara, SP 14801-907, Brazil

## Correspondence

Mateus M. Ferrer, Modeling and Molecular Simulations Group, São Paulo State University, UNESP, Bauru, SP 17033-360, Brazil.  
Email: mmferrer@yahoo.com.br

## Funding information

CAPES, Grant/Award Numbers: 787027/2013 and 8881068492/2014-01; FAPESP, Grant/Award Numbers: 2016/07476-9, 2013/07793-6 and 2013/19289-0; CNPq, Grant/Award Numbers: 46126-4 and 150936/2017-6

## Abstract

Theoretical and experimental methods were employed to investigate the vibrational modes of BiOBr. Wavenumber prediction and assignments of the infrared and Raman modes were performed using density functional theory and lattice dynamics calculations. The theoretical models were directly compared with the experimental results of particles fabricated using the microwave-assisted hydrothermal method and results reported in literature. The simulation results of the structure parameters, band gap, and vibrational modes are in agreement with the corresponding experimental values. The proposed models and calculations provided detailed insights into the vibrational modes and enabled to determine propagated assignment errors in results reported in the literature.

## KEYWORDS

BiOBr, density functional theory, GF-matrix, lattice dynamics calculation

## 1 | INTRODUCTION

Over the past decades, bismuth oxyhalides (where X = F, Cl, Br, or I) have been attracting research interests owing to their potentials for applications in several scientific fields.<sup>[1–3]</sup> Their particles exhibit a tetragonal matlockite structure, which can be considered part of the Sillen family. In particular, BiOBr presents exhibits promising semiconductor properties mainly for photocatalytic applications,<sup>[4,5]</sup> as well as other characteristics including

photoelectrochemical activity,<sup>[6]</sup> bacterial inactivation,<sup>[7]</sup> and photoluminescence.<sup>[8]</sup>

At ambient conditions, its structure is stable and it has a band gap energy ( $E_{\text{gap}}$ ) of  $\sim 2.7$  eV.<sup>[3]</sup> Furthermore, the particles can be easily produced using a large-scale fabrication process, which is an important factor for any material that has technological applications.<sup>[9]</sup>

BiOBr has been extensively investigated experimentally. Several studies characterized BiOBr synthesized through various methods producing particles with different structures

and properties.<sup>[10–12]</sup> However, the number of publications and targeted topics using theoretical approaches with quantum computational simulations for this system is not very high so far. Li et al. performed density functional theory (DFT) calculations to explain the efficient fixation of  $N_2$  to  $NH_3$  in BiOBr nanosheets without the presence of any organic scavenger or precious-metal cocatalysts.<sup>[13]</sup> In addition, Huang<sup>[14]</sup> and Huang and Zhu<sup>[15]</sup> employed DFT to evaluate the electronic levels (valence and conduction bands) of bismuth oxyhalides materials and modifications caused by the change of the halides.

Theoretical results can provide valuable information, which are often very challenging to be experimentally obtained, as it is the case for the electronic levels and fixation of a molecule in a solid. Therefore, theoretical approaches are of key importance for the understanding of the structural and electronic characteristics of materials, which can be employed to propose methods for the modulation of their properties. In many systems, using computational simulations, the characteristics including vibrational spectra, lattice parameters, and nanoparticles morphology can be obtained with a good accuracy.<sup>[16,17]</sup>

Regarding the vibrational modes of BiOBr, there are many studies that report infrared (IR) and Raman spectra measurements to reveal the active modes. However, the modes assignments and attribution come from few papers that indeed realize more elaborated attributions based on polarized Raman/IR measurements. Davies<sup>[18]</sup> performed an experimental evaluation of the IR and Raman modes; this paper is commonly cited as a reference for the determination of the modes of BiOBr. In his study, the analysis of the IR modes was performed by comparison with the modes of oriented films of BiOCl and BiOBr proposed by Rulmont.<sup>[19]</sup> In the case of Raman modes, Davies performed the attributions by comparison with BaClF and BaBrF materials, instead of performing a more precise determination.<sup>[20]</sup> To the best of our knowledge, Rulmont and Davies were the first researchers who

determined the IR and Raman modes of this material, respectively.

Therefore, there are several experimental studies with comparative indications; however, they lack discussions using theoretical approaches that provide a better understanding of the structural characterization of BiOBr.

In this study, we perform a detailed theoretical analysis with focus on the vibrational modes of BiOBr. Group theory, DFT, and lattice dynamics calculations (LDC) were performed in order to provide detailed insights into the structure motions and demonstrate propagated assignment errors in the literature about this system. The theoretical models were directly compared with experimental results of BiOBr particles synthesized using the microwave-assisted hydrothermal method.

## 2 | CRYSTAL STRUCTURE AND GROUP THEORY PREDICTIONS

At room temperature, BiOBr has a tetragonal cell that belongs to the space group  $P4/nmm$  ( $D_{4h}^7$ , No. 129). The crystal structure information were first reported by Bannister et al.<sup>[21]</sup> However, the structural data used as reference in this study were described by Kettler et al.<sup>[22]</sup> In this study, the primitive unit cell ( $Z = 2$ ) has lattice parameters of  $a = 3.923 \text{ \AA}$  and  $c = 8.105 \text{ \AA}$  (Figure 1a). The lattice can be regarded as alternate layers of  $Bi_2O_2$  clusters and double layers of halide along the [001] direction (Figure 1b). The double halide layers are connected by van der Waals interactions.<sup>[23]</sup> Considering the site occupations summarized in Table 1, the vibrational modes at the Brillouin zone center ( $\mathbf{q} \approx 0$ ) can be determined by the irreducible representation of the  $D_{4h}$  factor group, as listed in the last column of Table 1. Therefore, one should expect 4 IR-active ( $2A_{2u} \oplus 2E_u$ ) and 6 Raman-active ( $2A_{1g} \oplus B_{1g} \oplus 3E_g$ ) modes. We employed the nuclear site method developed by Rousseau et al. to predict the optical phonons features.<sup>[24]</sup> It is worth mentioning that the

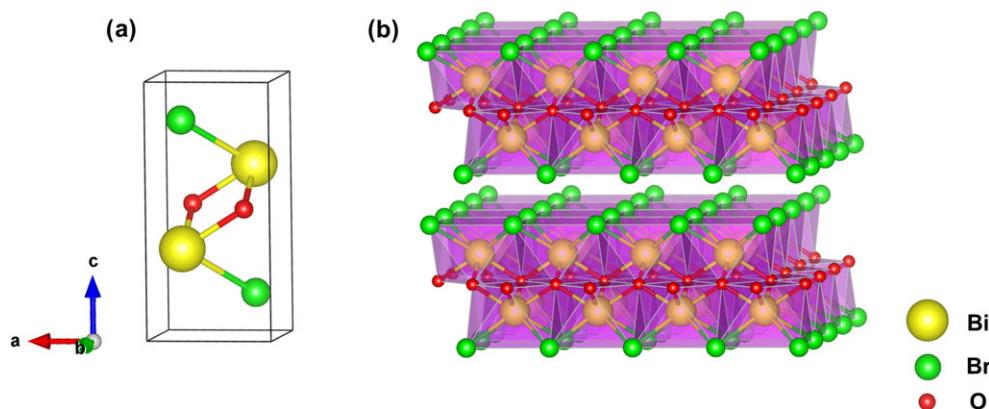


**FIGURE 1** Crystal structure representation of BiOBr: (a) atomic model for BiOBr used in the calculations and (b) BiOBr lattice showing the  $Bi_2O_2$  clusters and double layers of halides [Colour figure can be viewed at [wileyonlinelibrary.com](http://wileyonlinelibrary.com)]

**TABLE 1** Factor group analysis for the crystal structure of tetragonal BiOBr unit cell [Colour table can be viewed at wileyonlinelibrary.com]

Ion	Wyckoff site	Site symmetry	Fractional coordinates			Irreducible representation
			x	y	z	
Bi <sup>3+</sup>	2c	4 mm (C <sub>4v</sub> )	0.25	0.25	0.1540(1)	A <sub>1g</sub> ⊕ A <sub>2u</sub> ⊕ E <sub>g</sub> ⊕ E <sub>u</sub>
O <sup>2-</sup>	2a	-4 m2 (D <sub>2d</sub> )	0.25	0.75	0	A <sub>2u</sub> ⊕ B <sub>1g</sub> ⊕ E <sub>g</sub> ⊕ E <sub>u</sub>
Br <sup>1-</sup>	2c	4 mm (C <sub>4v</sub> )	0.25	0.25	0.6568(3)	A <sub>1g</sub> ⊕ A <sub>2u</sub> ⊕ E <sub>g</sub> ⊕ E <sub>u</sub>
Total						2A <sub>1g</sub> ⊕ 3A <sub>2u</sub> ⊕ B <sub>1g</sub> ⊕ 3E <sub>g</sub> ⊕ 3E <sub>u</sub>
Acoustic						A <sub>2u</sub> ⊕ E <sub>u</sub>
Silent						0
Infrared						2A <sub>2u</sub> ⊕ 2E <sub>u</sub>
Raman						2A <sub>1g</sub> ⊕ B <sub>1g</sub> ⊕ 3E <sub>g</sub>

Note. Atomic position and their respective site symmetry are summarized.

A- and B-type modes are nondegenerate, whereas the E-type modes are double-degenerate. The above subscripts “g” and “u” are related with the parity under the inversion operation in centrosymmetric crystals (e.g., BiOBr). The gerade (g) modes are Raman active modes, whereas the ungerade (u) modes are IR active modes.

### 3 | MATERIALS AND METHODS

#### 3.1 | Synthesis

BiOBr sample was fabricated using the microwave-assisted hydrothermal synthesis in the presence of amino acid as templates. First, 2.0 mmol of potassium bromide (KBr, 99% purity, Aldrich) and bismuth nitrate [Bi(NO<sub>3</sub>)<sub>3</sub>, 99% purity, Aldrich] were added to 100 ml of a 0.03-mol L<sup>-1</sup> solution of glycine. The mixture was stirred for 30 min, transferred to a 150-ml Teflon vessel placed in a stainless-steel autoclave reactor, and heated at 180 °C for 8 hr. The product was separated by centrifugation, washed with deionized water, and dried at 60 °C for 8 hr.

#### 3.2 | Characterization

X-ray diffraction (XRD) patterns were recorded to characterize the phase and structure of the as-prepared samples, using a D/Max-2500PC diffractometer (Rigaku, Japan)

operated at 40 kV and 150 mA, with a Cu-K<sub>α</sub> radiation (1.5406 Å), in the 2θ range of 7–90°. Raman spectrum at room temperature was recorded in a backscattering geometry using an HR800 evolution micro-Raman spectrometer (Horiba Jobin-Yvon). A 532-nm laser line was employed as the excitation source, recorded after the 50× objective. Prior to the fitting procedure, the as-recorded spectrum was corrected by the Bose–Einstein thermal factor [n(ω,T) + 1].<sup>[25]</sup> Near-IR spectrum at room temperature were recorded using a Bruker VERTEX 70 Fourier-transform IR spectrometer. The particle size and morphology were investigated using a Phenom ProX scanning electron microscope operated at 10 kV.

#### 3.3 | Quantum computational methods

The simulations for BiOBr were performed on a periodic cell using DFT with a B3LYP hybrid functional,<sup>[26,27]</sup> implemented on CRYSTAL14<sup>[28]</sup> program. Bismuth, oxygen, and bromine centers were described using the ECP60MFD\_s4411p411d411\_Heifets,<sup>[29]</sup> 8411(d11)\_Heifets,<sup>[29]</sup> and HAYWLC-31\_prenceipe, respectively.<sup>[30]</sup> All basis sets can be found at the CRYSTAL page (<http://www.crystal.unito.it/basis-sets.php>).

The calculations were performed with truncation criteria for the Coulomb and exchange series controlled by a set of five thresholds (10<sup>-8</sup>, 10<sup>-8</sup>, 10<sup>-8</sup>, 10<sup>-8</sup>, and

**TABLE 2** Interatomic force constant values derived after the lattice dynamics calculation

Force constant	Atoms involved	Multiplicity	Distance (Å)/angle (°)	Force constant value (md.Å <sup>-1</sup> )
K <sub>1</sub>	Bi(2c) – O(2a)	4	2.325	0.880
F <sub>1</sub>	Br(2c) – Br(2c)	4	3.763	0.142
H <sub>1</sub>	O(2a) – Bi(2c) – O(2a)	4	73.25	0.521
H <sub>2</sub>	Br(2c) – Bi(2c) – Br(2c)	4	76.46	1.517

$10^{-16}$ ), and shrinking factors (Pack-Monkhorst and Gilat net). The initial atomic positions and lattice parameters were set according to Ketterer et al.<sup>[22]</sup> The Raman and IR vibrational modes and their corresponding wavenumbers were calculated through numerical second derivatives of the total energy. The Raman and IR intensities were obtained through the CPHF/KS scheme.<sup>[31,32]</sup>

### 3.4 | Classical computational methods

Wilson's GF-matrix method was employed to perform LDC of the first-order Raman- and IR-active phonons for the tetragonal matlockite structure of BiOBr.<sup>[33]</sup> For the LDC, we employed the VIBRATZ software package developed by Dowty.<sup>[34]</sup>

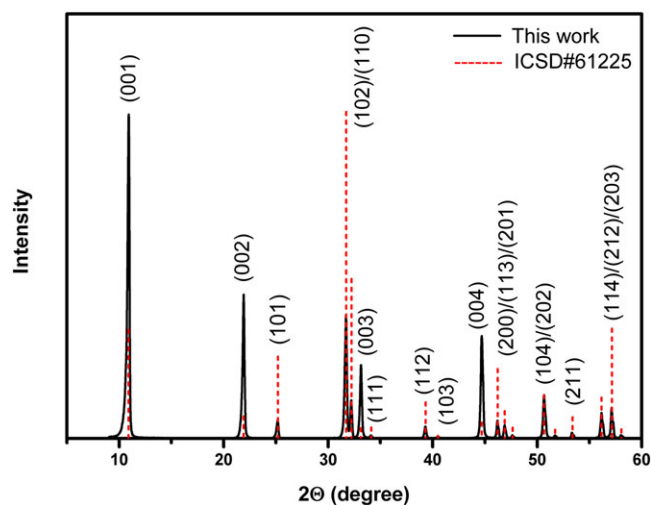


**FIGURE 2** X-ray diffraction at room temperature of the BiOBr microcrystals obtained by microwave-assisted hydrothermal method. The indices of planes are indexed in agreement with tetragonal structure following the ICSD card 61225. ICSD = inorganic crystal structure database [Colour figure can be viewed at [wileyonlinelibrary.com](http://wileyonlinelibrary.com)]

For accurate calculations of the vibrational wavenumbers, the short-range atomic interactions are required, including the valence ( $K_i$ ), repulsive ( $F_i$ ), and angle ( $H_i$ ) force constants. In this study, one valence, one repulsive, and two angle force constants are considered, as listed in Table 2. In addition, we obtained the individual contribution of each force constant to the optical phonons using the potential energy distribution (PED). This parameter provides a better understanding of the vibrational properties of the BiOBr structure.

## 4 | RESULTS AND DISCUSSION

All theoretical models were developed in comparison with experimental results of BiOBr obtained by the microwave-assisted hydrothermal method. Figure 2 shows the long-range crystalline information of BiOBr obtained using the XRD technique. The XRD pattern confirms the pure tetragonal structure (space group  $P4/nmm$ ), according to the inorganic crystal structure database (No. 61225).<sup>[22]</sup>

The short-range properties of the fabricated BiOBr were evaluated using Raman and IR spectroscopies, as shown in Figures 3 and 4, respectively.

A theoretical model of BiOBr was developed to evaluate the relationship between the structural vibrations and energy of the system. The structural and electronic characteristics of the model, including the optimized lattice parameters and band gap energy, are in a good agreement with the experimental results (Table S1 and Figures S1 and S2). The simulated Raman and IR spectra are also shown in Figures 3 and 4, respectively, without any scaling correction. Both experimental and theoretical spectra indicate the presence of six expected Raman-active modes in the range of 0–700  $\text{cm}^{-1}$  and four expected IR-active

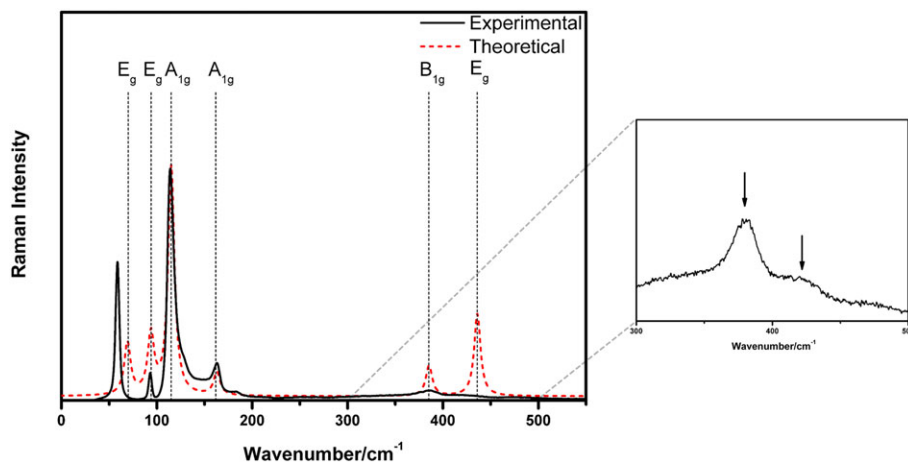


**FIGURE 3** Experimental and theoretical first-order Raman spectra of BiOBr at room temperature [Colour figure can be viewed at [wileyonlinelibrary.com](http://wileyonlinelibrary.com)]

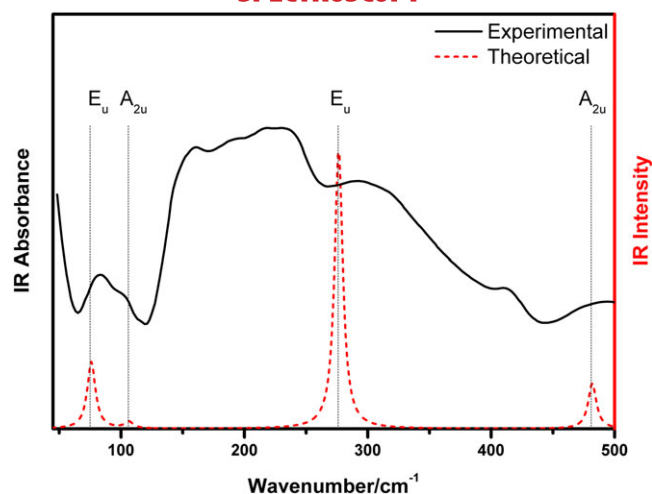


**FIGURE 4** Experimental and theoretical first-order IR spectra of BiOBr at room temperature [Colour figure can be viewed at [wileyonlinelibrary.com](http://wileyonlinelibrary.com)]

modes in the range of 0–550  $\text{cm}^{-1}$ , as expected for a pure crystalline sample according to the above group-theory predictions. All vibrational modes (theoretical and experimental) including the assignments from the DFT calculations are listed in Table 3.

The calculated Raman spectrum are in an excellent agreement with the experimental results in terms of the vibrational mode position; however, there are large difference in the mode position of lower wavenumber ( $\sim 60 \text{ cm}^{-1}$ ; Figure 3) with respect to other samples reported in the literature.<sup>[7,18]</sup> Figure S3 presents a careful decomposition process using Lorentzian profile functions of BiOBr Raman spectrum. In the decomposition, it is possible to observe additional modes most likely owing to the incorporation of impurities or structural local distortions. The

local symmetry breaking causes a loss of the inversion operation, which leads to an increased number of expected Raman-active modes.<sup>[35,36]</sup> The intensity predictions showed significant differences in the first and last two modes. In general, the simulated Raman profile has the same pattern of the experimental results. As the hydrothermal method for materials synthesis usually leads to a crystal growth with a preferential orientation,<sup>[37,38]</sup> we argued that our samples may have a partial preferential orientation, which explains the differences between some of the experimental and calculated Raman intensities. As one can note in the XRD data, it can be confirmed a tendency for a microcrystal growth along the [001] direction, because the experimental peak intensities of the (001), (002), (003), and (004) reflections are higher than those reported at the inorganic crystal structure database (i.e., completely random oriented; Figure 2). Figure S4 shows a scanning electron microscope image that confirms our assumption about the preferential orientation of the synthesized particles.

Regarding the IR data, the absorbance spectrum was overlapped with the simulated intensity of absorption of each mode. The theoretical mode positions were not obtained with the same accuracy as that in the Raman simulations; however, all simulated profiles are in agreement with the experimental results. Additional IR modes are observed in Figure 4, in accordance with the additional modes of Raman spectrum.

In general, the energies of the theoretical modes are very similar with the corresponding experimental values, which indicates the accuracy of the model and calculations. In order to compare our results, it was also included in Table 3 the wavenumbers of the vibrational modes and the assignment described by Davies; the study of Davies

**TABLE 3** Experimental Raman ( $A_{1g}$ ,  $B_{1g}$ , and  $E_g$ ) and IR ( $A_{2u}$  and  $E_u$ ) bands for the BiOBr tetragonal structure at room temperature, in which  $\tilde{\nu}$  are the phonon mode position ( $\text{cm}^{-1}$ )

Experimental <sup>a</sup> $\tilde{\nu}$ ( $\text{cm}^{-1}$ )	Ref (assignment) $\tilde{\nu}$ ( $\text{cm}^{-1}$ )	DFT (assignment) <sup>a</sup> $\tilde{\nu}$ ( $\text{cm}^{-1}$ )	LDC (assignment) <sup>a</sup>	
			$\tilde{\nu}$ ( $\text{cm}^{-1}$ )	PED $\geq 10\%$
59	57 ( $A_{1g}$ )	70 ( $E_g$ )	82 ( $E_g$ )	$K_1(16)$ , $F_1(28)$ , $H_1(57)$
93	92 ( $E_g$ )	98 ( $E_g$ )	123 ( $E_g$ )	$F_1(32)$ , $H_1(10)$ , $H_2(56)$
113	113 ( $A_{1g}$ )	115 ( $A_{1g}$ )	102 ( $A_{1g}$ )	$K_1(58)$ , $F_1(27)$ , $H_1(15)$
162	162 ( $E_g$ )	167 ( $A_{1g}$ )	145 ( $A_{1g}$ )	$K_1(10)$ , $F_1(39)$ , $H_2(49)$
384	385 ( $B_{1g}$ )	382 ( $B_{1g}$ )	328 ( $B_{1g}$ )	$K_1(100)$
425	410 ( $E_g$ )	429 ( $E_g$ )	436 ( $E_g$ )	$K_1(74)$ , $H_1(26)$
67	72 ( $E_u$ )	78 ( $E_u$ )	91 ( $E_u$ )	$H_2(99)$
121	125 ( $A_{2u}$ )	106 ( $A_{2u}$ )	100 ( $A_{2u}$ )	$H_2(99)$
276	265 ( $E_u$ )	274 ( $E_u$ )	401 ( $E_u$ )	$K_1(89)$ , $H_1(11)$
445	512 ( $A_{2u}$ )	481 ( $A_{2u}$ )	380 ( $A_{2u}$ )	$K_1(80)$ , $H_1(19)$

<sup>a</sup>This work.

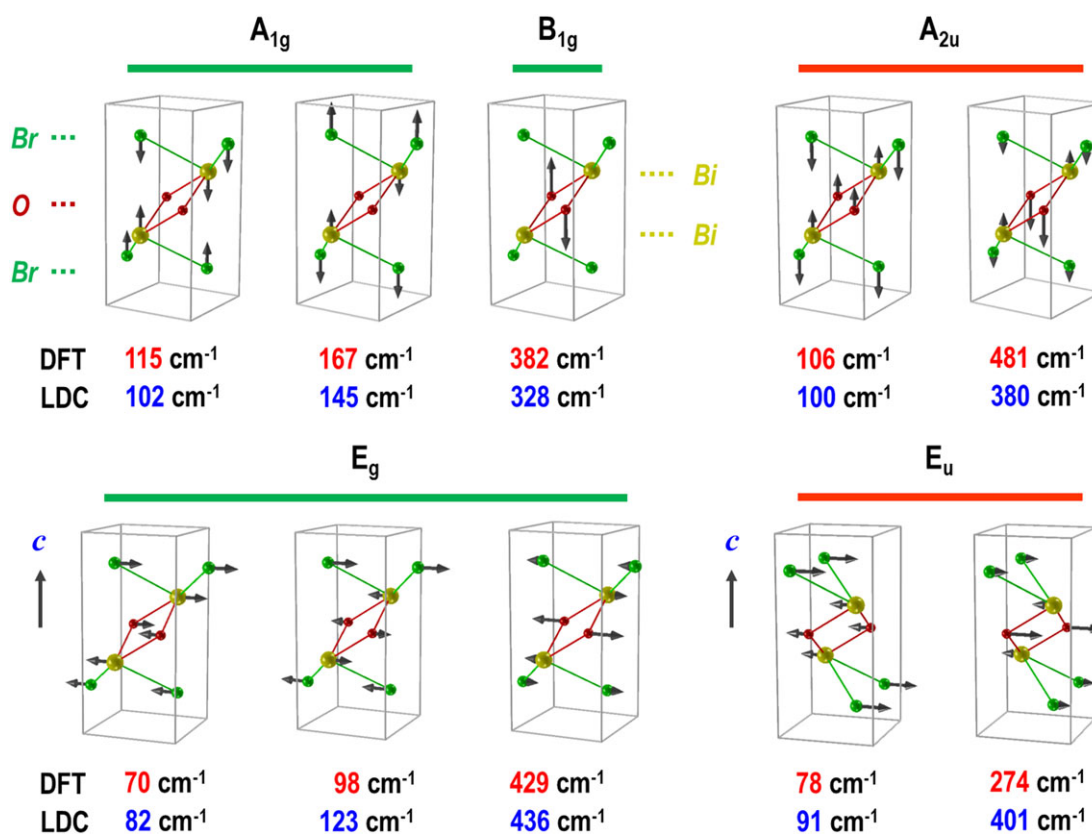
on the BiOBr vibrational modes, as mentioned above, was used in many reports as a reference to identify the vibrational modes.

Table 3 shows that BiOBr modes' wavenumbers reported by Davies are very similar to our results. However, there are differences in the assignment obtained by the DFT calculations with respect to those reported by Davies and, consequently, other studies that used his results as a reference. These reports suggested that the first and fourth active modes around 60 and 160  $\text{cm}^{-1}$  are  $A_{1g}$  and  $E_g$  modes, respectively. The quantum computations showed an inversion, where the first is  $E_g$ , whereas the fourth is  $A_{1g}$  mode. This represents an inversion of symmetry of the species, where the first mode at 60  $\text{cm}^{-1}$  is actually two-fold degenerated with respect to  $C_n$ , whereas the fourth mode is symmetric with respect to  $C_n$  and  $S_n$ . Experimental results that correspond to our theoretical prediction are reported in the paper of Rulmont about polarized Raman studies on the BiOCl single crystal.<sup>[39]</sup> In particular, the author attributed the  $E_g$  symmetry to the mode at 59  $\text{cm}^{-1}$ . This mode is similar to that of BiOBr at 57  $\text{cm}^{-1}$ , reported in Davies's study.

The LDC method was employed in order to compare and confirm our first affirmations based on the DFT calculations and better describe the modes. Therefore, using

the set of force constants listed in Table 2, we calculated the Raman and IR wavenumbers at the zone center. The LDC results are summarized in Table 3.

The comparison with the experimental results shows that there is a good agreement with both DFT- and LDC-calculated Raman and IR bands. The LDC results also mean that the vibrational spectra can be simply described using the short-range force constants. The atomic displacement patterns that represent the optical modes (Raman and IR) are illustrated in Figure 5 (see also the 2D projection [Figure S5] and Video S1). The  $A_{1g}$  modes correspond to the motions of  $\text{Bi}_2\text{O}_2$  clusters and double layers of halide along the  $c$ -axis of the  $D_{4h}$  tetragonal cell. In particular, the  $A_{1g}$  mode centered at  $\sim 102 \text{ cm}^{-1}$  (calculated using LDC) has a high intensity in the Raman spectra, in agreement with the DFT results. This mode can be regarded as a compression-type movement of the  $\text{Bi}_2\text{O}_2$  cluster layers and double halide layers, where the major contribution is from the Bi–O bond ( $K_1$  force constant; see the PED values [ $\sim 58\%$  for  $K_1$ ] in the last column of Table 3). Indeed, the Raman bands with wavenumber values below 200  $\text{cm}^{-1}$  are very halogen-dependent. It is worth mentioning that the  $B_{1g}$  mode has a major contribution from the  $K_1$  force constant, where only oxygen atoms are allowed to move.



**FIGURE 5** Atomic displacements of six Raman-active ( $A_{1g}$ ,  $B_{1g}$ , and  $E_g$ ) modes and four IR-active ( $A_{2u}$  and  $E_u$ ) ones for BiOBr tetragonal structure. DFT = density functional theory; LDC = lattice dynamics calculations [Colour figure can be viewed at [wileyonlinelibrary.com](http://wileyonlinelibrary.com)]

The  $E_g$  modes are related with the movements of all atoms at the  $ab$ -plane, while maintaining the inversion operation. It is worth mentioning the high wavenumber  $E_g$  mode centered at  $436\text{ cm}^{-1}$  (determined using LDC) with a low Raman intensity in the experimental spectrum shown in Figure 3. For systems with well-defined external and internal modes, the high wavenumber Raman bands correspond to high intensity modes, as observed in ordered perovskites.<sup>[40]</sup> Their Raman spectra consist of two distinctive regions, a low-wavenumber part that corresponds to the translational movements of the heavier atoms and a high-wavenumber part that corresponds to the internal vibrations of the pure octahedra (for perovskites). Then, the most intense Raman mode usually represents the symmetrical stretching vibration of the octahedra (or breathing mode).<sup>[41]</sup> For BiOBr, there is no way to separate the atomic displacements in those two parts by identifying the octahedral and tetrahedral groups. Further, the structural constrains may be the reason behind the low intensity observed for the  $E_g$  mode at  $436\text{ cm}^{-1}$ , besides its asymmetrical origin, as illustrated in Figure 5.

The more intense IR band (at  $274\text{ cm}^{-1}$  by DFT and  $401\text{ cm}^{-1}$  by LDC) in the theoretical spectrum is attributed to the vibrations of oxygen ions towards the  $ab$ -plane, which involve mainly the  $K_1$  force constant (89% in its PED). Figure 5 shows that the oxygen displacements are in opposite direction with respect to that of Bi. We can propose that any local symmetry breaking in the  $\text{Bi}_2\text{O}_2$  clusters concerning the Bi–O bonds could be identified by analyzing the IR band centered at  $276\text{ cm}^{-1}$  ( $E_u$ ). On the other hand, the  $A_{2u}$  modes correspond to atomic displacements along the  $c$ -axis of the tetragonal cell with a tendency to form a polar axis in this direction. These IR nondegenerate modes mainly involve Br and O atoms, as illustrated in Figure 5.

## 5 | CONCLUSIONS

An accurate analysis of the vibrational modes of BiOBr was performed in order to provide insights into the structure and motion of BiOBr upon absorption of energy. All Raman and IR active modes were evaluated using quantum and classical methods based on DFT and LDC, respectively. Theoretical spectra were simulated through the CPHF/KS scheme incorporated in the CRYSTAL14 software package. Experimental BiOBr sample was synthesized using the microwave-assisted hydrothermal method to directly compare the experimental and theoretical spectra, and with results reported in literature. In addition to the assignment of modes, the presence of propagated errors in the literature was demonstrated for

the modes at  $60$  and  $160\text{ cm}^{-1}$ . Both quantum and classical calculations showed that the modes are actually  $E_g$  and  $A_{1g}$ , respectively; opposite of the behavior showed in the reference papers on the vibrational modes of this material. The knowledge about the vibrational modes is of key importance for a proper correlation between the structural changes and response that determines the properties of this material.

## ACKNOWLEDGEMENTS

This work was supported by Brazilian funding agencies: CNPq (46126-4, 150936/2017-6), CAPES (787027/2013, 8881068492/2014-01), FAPESP (2013/19289-0, 2013/07793-6, 2016/07476-9) and FAPEMIG (APQ-03589-16). The computational facilities were supported by resources supplied by Molecular Simulations Laboratory, São Paulo State University, Bauru, Brazil.

## ORCID

Mateus M. Ferrer  <http://orcid.org/0000-0002-0484-0192>  
 João Elias F.S. Rodrigues  <http://orcid.org/0000-0002-9220-5809>

## REFERENCES

- [1] J. Cao, B. Xu, B. Luo, H. Lin, S. Chen, *Catal. Commun.* **2011**, *13*, 63.
- [2] N. Kijima, K. Matano, M. Saito, T. Oikawa, T. Konishi, H. Yasuda, T. Sato, Y. Yoshimura, *Appl. Catal., A* **2001**, *206*, 237.
- [3] H. Cheng, B. Huang, Y. Dai, *Nanoscale* **2014**, *6*, 2009.
- [4] Z. Jiang, F. Yang, G. Yang, L. Kong, M. O. Jones, T. Xiao, P. P. Edwards, *J. Photochem. Photobiol., A* **2010**, *212*, 8.
- [5] Y. Huo, J. Zhang, M. Miao, Y. Jin, *Appl. Catal., B* **2012**, *111*, 334.
- [6] D. S. Bhachu, S. J. A. Moniz, S. Sathasivam, D. O. Scanlon, A. Walsh, S. M. Bawaked, M. Mokhtar, A. Y. Obaid, I. P. Parkin, J. Tang, C. J. Carmalt, *Chem. Sci.* **2016**, *7*, 4832.
- [7] D. Wu, B. Wang, W. Wang, T. An, G. Li, T. W. Ng, H. Y. Yip, C. Xiong, H. K. Lee, P. K. Wong, *J. Mater. Chem. A* **2015**, *3*, 15148.
- [8] R. Saraf, C. Shivakumara, S. Behera, N. Dhananjaya, H. Nagabhushana, *RSC Adv.* **2015**, *5*, 9241.
- [9] J. Zhang, F. Shi, J. Lin, D. Chen, J. Gao, Z. Huang, X. Ding, C. Tang, *Chem. Mater.* **2008**, *20*, 2937.
- [10] Y. Feng, L. Li, J. Li, J. Wang, L. Liu, *J. Hazard. Mater.* **2011**, *192*, 538.
- [11] Y. Chen, M. Wen, Q. Wu, *CrystEngComm* **2011**, *13*, 3035.
- [12] D. Zhang, J. Li, Q. Wang, Q. Wu, *J. Mater. Chem. A* **2013**, *1*, 8622.
- [13] H. Li, J. Shang, Z. Ai, L. Zhang, *J. Am. Chem. Soc.* **2015**, *137*, 6393.
- [14] W. L. Huang, *J. Comput. Chem.* **2009**, *30*, 1882.
- [15] W. L. Huang, Q. Zhu, *J. Comput. Chem.* **2009**, *30*, 183.



- [16] T. M. Duarte, P. G. C. Buzolin, I. M. G. Santos, E. Longo, J. R. Sambrano, *Theor. Chem. Acc.* **2016**, *135*, 151.
- [17] P. F. S. Pereira, C. C. Santos, A. F. Gouveia, M. M. Ferrer, I. M. Pinatti, G. Botelho, J. R. Sambrano, I. L. V. Rosa, J. Andrés, E. Longo, *Inorg. Chem.* **2017**, *56*, 7360.
- [18] J. E. D. Davies, *J. Inorg. Nucl. Chem.* **1973**, *35*, 1531.
- [19] A. Rulmont, *Spectrochim. Acta A* **1972**, *28*, 1287.
- [20] J. F. Scott, *J. Chem. Phys.* **1968**, *49*, 2766.
- [21] F. A. Bannister, M. H. Hey, *Mineral. Mag.* **1935**, *24*, 49.
- [22] J. Ketterer, V. Kramer, *Acta Crystallogr. C* **1986**, *42*, 1098.
- [23] H. Deng, J. Wang, Q. Peng, X. Wang, Y. Li, *Chem. – Eur. J.* **2005**, *11*, 6519.
- [24] D. L. Rousseau, R. P. Bauman, S. P. S. Porto, *J. Raman Spectrosc.* **1981**, *10*, 253.
- [25] D. A. Long, *The Raman Effect: A Unified Treatment of the Theory of Raman Scattering by Molecules*, John Wiley & Sons, West Sussex, England **2002**.
- [26] A. D. Becke, *J. Chem. Phys.* **1993**, *98*, 5648.
- [27] C. Lee, W. Yang, R. G. Parr, *Phys. Rev. B* **1988**, *37*, 785.
- [28] R. Dovesi, R. Orlando, A. Erba, C. M. Zicovich-Wilson, B. Civalleri, S. Casassa, L. Maschio, M. Ferrabone, M. De La Pierre, P. D'Arco, Y. Noël, M. Causà, M. Rérat, B. Kirtman, *Int. J. Quantum Chem.* **2014**, *114*, 1287.
- [29] E. Heifets, E. Kotomin, A. Bagaturyants, J. Maier, *J. Phys. Chem. Lett.* **2015**, *6*, 2847.
- [30] M. Prencipe, Laurea Thesis (Laurea University of Applied Sciences, Vantaa, Finland) **1990**; 87.
- [31] L. Maschio, B. Kirtman, R. Orlando, M. Rérat, *J. Chem. Phys.* **2012**, *137*, 204113.
- [32] L. Maschio, B. Kirtman, M. Rérat, R. Orlando, R. Dovesi, *J. Chem. Phys.* **2013**, *139*, 164101.
- [33] E. B. Wilson, J. C. Decius, P. C. Cross, *Molecular Vibrations: The Theory of Infrared and Raman Vibrational Spectra*, Dover Publications, New York **1955**.
- [34] E. Dowty, *Phys. Chem. Miner.* **1987**, *14*, 122.
- [35] S. P. Marcondes, J. E. F. S. Rodrigues, M. R. B. Andreetta, A. C. Hernandez, *Vib. Spectrosc.* **2014**, *73*, 144.
- [36] A. P. Ayala, C. W. A. Paschoal, I. Guedes, W. Paraguassu, P. T. C. Freire, J. Mendes Filho, R. L. Moreira, J. Y. Gesland, *Phys. Rev. B* **2002**, *66*, 214105.
- [37] M. A. P. Almeida, L. S. Cavalcante, C. Morilla-Santos, C. J. Dalmaschio, S. Rajagopal, M. S. Li, E. Longo, *CrystEngComm* **2012**, *14*, 7127.
- [38] S. Baruah, J. Dutta, *Sci. Technol. Adv. Mater.* **2009**, *10*, 013001.
- [39] A. Rulmont, *Spectrochim. Acta A* **1974**, *30*, 311.
- [40] A. P. Ayala, I. Guedes, E. N. Silva, M. S. Augsburg, M. Del, C. Viola, J. C. Pedregosa, *J. Appl. Phys.* **2007**, *101*, 123511.
- [41] C. L. Diao, C. H. Wang, N. N. Luo, Z. M. Qi, T. Shao, Y. Y. Wang, J. Lu, Q. C. Wang, X. J. Kuang, L. Fang, F. Shi, X. P. Jing, *J. Appl. Phys.* **2014**, *115*, 114103.

## SUPPORTING INFORMATION

Additional Supporting Information may be found online in the supporting information tab for this article.

**How to cite this article:** Ferrer MM, Rodrigues JEFS, Almeida MAP, et al. Theoretical methods for calculations of optical phonons in BiOBr: Analysis and correction of propagated errors. *J Raman Spectrosc.* 2018;49:1356–1363. <https://doi.org/10.1002/jrs.5377>